# Proton dynamics in oxides: insight into the mechanics of proton conduction from quasielastic neutron scattering


| | |
|---|---|
| Journal: | *Physical Chemistry Chemical Physics* |
| Manuscript ID: | CP-PER-09-2014-004112.R1 |
| Article Type: | Perspective |
| Date Submitted by the Author: | 10-Oct-2014 |
| Complete List of Authors: | Karlsson, Maths; Chalmers University of Technology, Applied Physics |
| | |


Physical Chemistry Chemical Physics
CREATED USING THE RSC LaTeX PCCP ARTICLE TEMPLATE – SEE www.rsc.org/electronicfiles FOR DETAILS
ARTICLE TYPE www. rsc.org/xxxxxx | XXXXXXXX

# Proton dynamics in oxides: insight into the mechanics of proton conduction from quasielastic neutron scattering

**Maths Karlsson***

*Received Xth XXXXXXXXXX 20XX, Accepted Xth XXXXXXXXX 20XX*
*First published on the web Xth XXXXXXXXXX 200X* **DOI: 10.1039/b000000x**

This article is concerned with the use of quasielastic neutron scattering as a technique for investigations of the dynamical properties of proton conducting oxides. Currently, the main interest in these materials comes from their promise as electrolytes in future electrochemical devices and particularly through their use as electrolytes in next-generation, intermediate-temperature, fuel cells. However, the realization of such devices depends critically on the development of new, more highly proton conducting oxides. Such a development depends on increasing the current understanding of proton conduction in oxides and for this purpose quasielastic neutron scattering is an important mean. The aim of this article is to introduce the non-specialist reader to the basic principles of quasielastic neutron scattering, its advantages and disadvantages, to summarize the work that has been done on proton conducting oxides using this technique, as well as to discuss future opportunities within this field of research.

## 1 Introduction

Neutron scattering is now a well-established technique in the field of solid state ionics, *i.e.* the study of solid electrolytes and their uses, and have played a crucial role in contributing to the current understanding of ion conducting solids. This encompasses studies both of crystal structures, *via* neutron diffraction (ND), surface and near-surface phenomena *via* neutron reflectivity (NR), as well as of the dynamical nature of materials *via* inelastic and quasielastic neutron scattering (INS and QENS). Whereas the majority of previous neutron work has focussed on structural investigations using ND techniques, less work has been directed towards dynamical studies using INS and QENS.

This article is specifically concerned with the application of QENS for dynamical studies of proton conducting oxides. The primary interest in these materials, which may be classified according to their structure type, comes from their potential to contribute to a sustainable future, in particular through their use as electrolytes in next-generation, intermediate-temperature (≈200–500 °C) solid oxide fuel-cell (SOFC) technology,[1–3] as well as through their use as electrolytes in hydrogen sensors and through their relatively unexplored potential as catalytic materials.[4]

A particularly promising class of proton conducting oxides are $ABO_3$-type perovskites, where $A$ is a relatively large cation, with oxidation state commonly +2, and $B$ is a cation with oxidation state commonly +4.[2] The incorporation of protons into these structures relies on acceptor doping to the $B$ site, such as $Y^{3+}$ substituted for $Ce^{4+}$ in $BaCeO_3$, followed by hydration. The acceptor doping creates oxygen vacancies, which can be subsequently filled with oxygens during the hydration procedure.[2] The hydration is usually performed by heat treatment of the sample in a humid atmosphere; a process during which the water molecules in the gaseous phase dissociate into hydroxyl groups (-$OH^-$) and protons ($H^+$) on the surface of the sample. The -$OH^-$ groups then stick to nearby oxygen vacancies, whereas the (other) protons bind to lattice oxygens of the oxide host lattice. In Kröger-Vink notation[5] this reaction may be written

$$H_2O + V_O^{\cdot\cdot} + O_O^{\times} \Leftrightarrow 2(OH_O^{\cdot}), \quad (1)$$

where $V_O^{\cdot\cdot}$ denotes an oxygen vacancy, $O_O^{\times}$ denotes a lattice oxygen, and $OH_O^{\cdot}$ denotes a proton bound to a lattice oxygen (the superscripts $^{\cdot}$ and $^{\times}$ denote positive and neutral charges, respectively).

The protons are not stuck to any particular oxygens, but are rather free to move from one oxygen to another one and with time they will therefore diffuse into the bulk of the material. At the same time as protons diffuse into the bulk, the counter diffusion of oxygen vacancies from the bulk to the surface allows the dissociation of other water molecules on the surface of the sample. This leads to an increase of the proton concentration in the material, and so it is believed that the process continues until most, if not all, of the (bulk) oxygen vacancies are filled.

The incorporation of protons during hydration in itself means that the protons have to be mobile. The mobility of protons is routinely characterized by impedance spectroscopy techniques, with which the conductivity of protons can be determined on a macroscopic length-scale. In the case of poly-

Department of Applied Physics, Chalmers University of Technology, SE-412 96 Göteborg, Sweden. Fax: +46 31 772 2090; Tel: +46 31 772 8038; E-mail: maths.karlsson@chalmers.se

crystalline samples, the impedance spectra may allow the separation of bulk conductivity from contributions from the grain boundaries (GBs). The conductivity in GBs is lower than in the bulk. This is thought to be due to either a structural misalignment in the GB region, leading to lower proton conductivity, or the appearance of a space-charge layer around the GB core, which leads to Schottky barriers and the depletion of mobile protons. At present the latter explanation is the predominating one,[6,7] but the details of the GB core are not fully understood.

The connection between macroscopic proton conductivity, $\sigma$, and proton diffusion coefficient, $D_\sigma$, is given by the Nernst-Einstein equation

$$D_\sigma = \sigma(T)\frac{k_B T}{e^2 N}, \quad (2)$$

where $k_B$ is the Boltzmann constant, $T$ the temperature, $e$ the proton charge, and $N$ the number density of the mobile protons. The proton diffusion coefficient, $D_\sigma$, is proportional to the proton self-diffusion coefficient, $D_s$, *via* the Haven ratio $H_R = D_s/D_\sigma$. The Haven ratio, which may have values both smaller or larger than 1, reflects correlation effects, such as deviations from directional and/or temporal randomness of consecutive proton jumps, whereas $D_s$ is the quantity that is normally measured in QENS experiments. QENS can give information about both the time-scale and spatial geometry of dynamical processes, which is unique compared to other spectroscopic techniques. This deeper understanding of the dynamical aspects of the proton diffusion is achieved through the analysis of the momentum and energy transferred in the scattering event.

The aim of this article is to introduce the non-specialist reader to the basic concepts of QENS, its advantages and disadvantages, and to review the QENS studies that have been done on proton conducting oxides so far, as well as to discuss the state of the art and prospectives and importance for future work in this field. Articles concerned with the use of neutron scattering techniques for studies of solid state ionics in a wider context and not specialized on QENS, are reported elsewhere.[8,9]

## 2 Neutron scattering experiments

### 2.1 Neutron sources and the production of free neutrons

Neutron scattering experiments are performed at large-scale neutron scattering facilities, where neutrons are produced either by nuclear fission or by spallation. In nuclear fission, certain isotopes of very heavy elements, such as uranium or plutonium, are bombarded with neutrons during which other neutrons, as well as a great deal of energy, are released from the nuclei of the isotopes. If the free neutrons are let to react with other atoms, then even more neutrons are released and as a consequence a self-sustaining chain reaction is created. In spallation sources, on the other hand, neutrons are released (spallated) by the bombardment of protons on a heavy metal target. In both types of neutron sources, the produced neutrons are of very high energy (MeV), much higher than what is useful for neutron scattering experiments. The neutrons are therefore slowed down in a, so called, moderator, before they are guided to large instrument halls containing instruments designed for certain types of experiments. The type and temperature of the moderator determine the energy of the neutrons. Generally, neutron energies in the range 0.1–10 meV refer to cold neutrons, neutron energies in the range 10–100 meV refer to thermal neutrons, and neutron energies in the range 100–1000 meV refer to hot neutrons. Cold and thermal neutrons are particularly useful in QENS experiments, since their energies and wavelengths match the energies of relevant dynamical processes and interatomic distances in condensed matter. The implication of this is two-fold: firstly, it implies that the scattered neutrons may take up or loose a large part of their incoming energy, which means that dynamics can be measured with high accuracy; secondly, it implies that interference effects of the scattered neutrons occur, which gives structural information. Furthermore, the interaction of neutrons with matter is for most materials weak, which ensures that the bulk sample is being probed and not just surface or near-surface states that may behave differently from the bulk.

Examples of state of the art neutron research reactors are the Institut Laue-Langevin (ILL) in France, the NIST Centre for Neutron Research (NCNR) in the US, the Laboratoire Léon Brillouin (LLB) in France, the FRM-II facility in Germany, and the OPAL neutron source of the Australian Nuclear Science and Technology Organisation (ANSTO), which are all continuous neutron sources, whereas the IBR-2M reactor of the Frank Laboratory of Nuclear Research in Russia is a pulsed source. Examples of spallation sources are the ISIS neutron facility in the UK, the Spallation Neutron Source (SNS) in the US, and the Japan Proton Accelerator Research Complex (J-PARC) in Japan, which are pulsed sources, and the Swiss Spallation Neutron Source (SINQ) in Switzerland which is a continuous source. The next-generation neutron source is the European Spallation Source (ESS), a pulsed source which is being constructed in Sweden and that will come into operation around 2020.

### 2.2 Scattering theory and scattering cross sections

As in all scattering experiments, the energy and momentum are conserved during a neutron scattering event. The energy of a neutron is given by $E = \hbar^2 k^2/2m$, where $m$ is the neutron's mass and $k$ is the magnitude of the associated wave vector, $|\boldsymbol{k}| = k = 2\pi/\lambda$, and $\lambda$ is the wavelength of the neutron. Ex-

pressions for the momentum and energy transferred from the sample to the neutron during the scattering event may then be written as

$$\hbar \boldsymbol{Q} = \hbar(\boldsymbol{k}_0 - \boldsymbol{k}_1), \tag{3}$$

$$|Q|^2 = |k_0|^2 + |k_1|^2 - 2|k_0||k_1|\cos 2\theta, \tag{4}$$

and

$$\hbar\omega = E_0 - E_1 = \frac{\hbar^2}{2m}(|k_0|^2 - |k_1|^2), \tag{5}$$

where $\boldsymbol{k}_0$ and $E_0$ are the wave vector and energy of the incident neutron and $\boldsymbol{k}_1$ and $E_1$ that of the scattered, and $2\theta$ is the scattering angle. As the vast majority of QENS studies of proton conducting oxides are done on powder samples, which do not have any preferred orientation, all that generally matters is the magnitude of $\boldsymbol{Q}$. Therefore, the vector character of $\boldsymbol{Q}$ is ignored in the following.

The measured quantity in most experiments is the double differential scattering cross section, $\mathrm{d}^2\sigma/\mathrm{d}\Omega\mathrm{d}E$, which represents the number of neutrons scattered into the solid angle $\mathrm{d}\Omega$ with energy in the range $\mathrm{d}E$. The amplitude of the scattered wave depends on the type of nuclei on which the neutrons are scattered and is also isotope and spin dependent, thus averages have to be taken for each element. The total cross section per scatterer, $\sigma$, reflects the effective areas of nuclei as seen by the incident neutrons and is obtained by integrating over all energies and solid angles,

$$\sigma = \int \mathrm{d}E \int \mathrm{d}\Omega \frac{\mathrm{d}^2\sigma}{\mathrm{d}\Omega\mathrm{d}E} = 4\pi\langle b^2\rangle. \tag{6}$$

Here $b$ is the scattering length, which can be either real or complex. The real part is usually positive (with the notable exception of H, which has a negative scattering length) and means a repulsive potential between the neutron and nucleus, whereas a negative scattering length means that the neutron is subjected to an attractive potential. The imaginary part relates to the probability that the neutron is absorbed rather than scattered.

The total scattering cross section can be split into coherent and incoherent parts. The coherent part, $\sigma_{\mathrm{coh}}$, corresponds to an average over all isotopes and nuclear spin states and may be written as

$$\sigma_{\mathrm{coh}} = 4\pi\langle b\rangle^2 = 4\pi b_{\mathrm{coh}}^2. \tag{7}$$

The incoherent part, $\sigma_{\mathrm{inc}}$, corresponds to the difference between the total and coherent scattering cross sections and is given by

$$\sigma_{\mathrm{inc}} = 4\pi(\langle b^2\rangle - \langle b\rangle^2). \tag{8}$$

It represents therefore the mean square deviation from the mean potential, which is due to isotopic and/or spin dependent effects of the scattering length.

As in the case for the scattering cross sections, the measured quantity in neutron scattering experiments, *i.e.* the double differential scattering cross section, can be separated into one coherent and one incoherent part according to

$$\frac{\mathrm{d}^2\sigma}{\mathrm{d}\Omega\mathrm{d}E} = \frac{k_0}{k_1}\frac{1}{4\pi\hbar}\left[\sigma_{\mathrm{coh}}S_{\mathrm{coh}}(Q,\omega) + \sigma_{\mathrm{inc}}S_{\mathrm{inc}}(Q,\omega)\right]. \tag{9}$$

Here $S_{\mathrm{coh}}(Q,\omega)$ and $S_{\mathrm{inc}}(Q,\omega)$ are known as the coherent and incoherent dynamical structure factors, respectively, which are the functions measured in most QENS experiments. The coherent part gives information about interference effects in materials, thus it provides information about the behavior of atoms in relation to each other, whereas the incoherent part relates to scattering from individual atoms. The Fourier transforms of $S_{\mathrm{coh}}(Q,\omega)$ and $S_{\mathrm{inc}}(Q,\omega)$, give the so-called intermediate scattering functions, $I_{\mathrm{coh}}(Q,t)$ and $I_{\mathrm{inc}}(Q,t)$, which in turn are the Fourier transforms of the total and self real-space time correlation functions, $G(r,t)$ and $G_{\mathrm{self}}(\mathrm{r},t)$, such that

$$G(r,t) = \frac{\hbar}{(2\pi)^3}\int\int S_{\mathrm{coh}}(Q,\omega)e^{-i(Q\cdot r-\omega\cdot t)}dQd\omega, \tag{10}$$

and

$$G_{\mathrm{self}}(r,t) = \frac{\hbar}{(2\pi)^3}\int\int S_{\mathrm{inc}}(Q,\omega)e^{-i(Q\cdot r-\omega\cdot t)}dQd\omega. \tag{11}$$

$G(r,t)$ gives the probability that given an atom at the origin at time $t = 0$, the same or any other atom will be found at a position $r$ at a later time $t$. $G_{\mathrm{self}}(r,t)$ gives the probability that the same particle will be found at the position $r$ at a later time $t$. Finally, one should note that since $r$ and $t$ are the Fourier-transformed variables of $Q$ and $\omega$, long distances in real space correspond to small $Q$, and *vice versa*. Analogously, slow diffusivities, implying long times in $G(r,t)$, correspond to small $\omega$.

### 2.3 Quasielastic neutron scattering

QENS refers to those inelastic processes that are almost elastic. The term is usually considered to mean a broadening of the elastic line in the neutron energy spectrum, $S(Q,\omega)$, rather than the appearance of discrete peaks associated with inelastic scattering.* This is illustrated schematically in Fig. 1. The elastic component is due to scattering from atoms which are localized in space, or in other words move too slowly to be resolved within the resolution of the instrument. The inelastic peaks arise from scattering from atoms which vibrate in a periodic manner and with a fixed frequency. Analogously to

* However, in case the intermediate scattering function, $I(Q,t)$, is measured, as is the case in neutron spin-echo experiments, the quasielastic scattering is manifested as a relaxational decay with time.

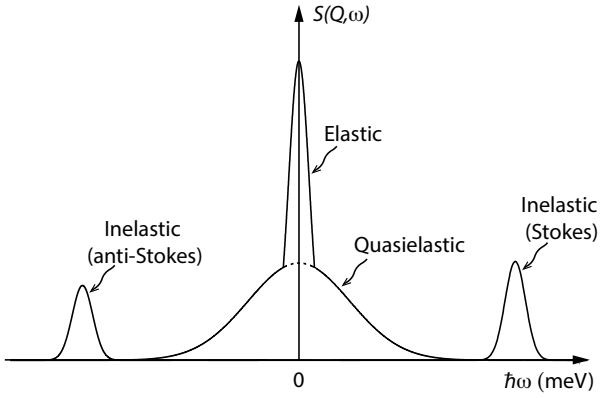


**Fig. 1** Schematic illustration of a neutron scattering spectrum, containing elastic, inelastic, and quasielastic components. The inelastic scattering has contributions from Stokes (neutron energy loss) and anti-Stokes (neutron energy gain) scattering, respectively. Although purely elastic scattering is defined as $\hbar\omega = 0$, every instrument has a finite resolution and therefore the elastic component has here been broadened to reflect this.

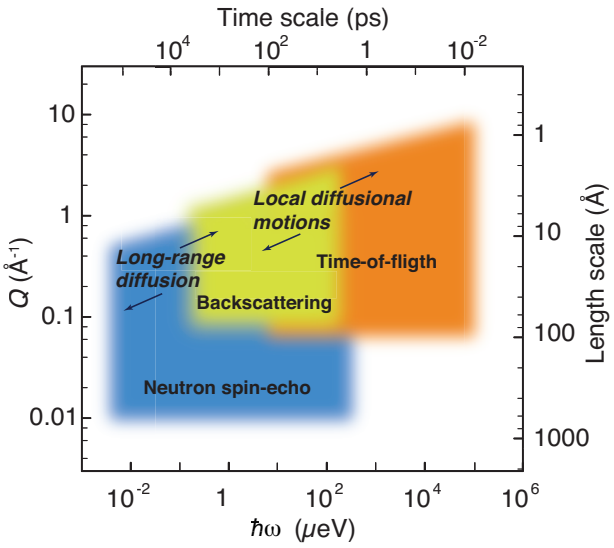


**Fig. 2** Neutron spectroscopy methods at the ILL encompass a large range of time- and length-scales. The $(Q,\hbar\omega)$ ranges of relevance for dynamical processes in proton conducting oxides are indicated. The figure has been modified after Jobic *et al.* [10].

inelastic light scattering (by Raman spectroscopy), the inelastically scattered neutrons can either loose energy (Stokes scattering) or gain energy (anti-Stokes scattering), respectively, however, in comparison to its optical counterpart, INS does not rely on any selection rules.† The QENS broadening is due to scattering from atoms that are moving in a stochastic manner.

Just as for other kinds of neutron scattering, QENS contains both coherent and incoherent scattering contributions. As mentioned above, the coherent scattering yields information about interference phenomena between atoms, which in QENS measurements means that information about collective dynamics, *e.g.* transport properties, may be obtained. The incoherent scattering, on the contrary, relates to scattering from individual atoms, thus providing information about single-particle motions, also known as self-dynamics.

## 2.4 QENS techniques

QENS techniques can be largely grouped into time-of-flight, backscattering, and neutron spin-echo (NSE) spectroscopy. The majority of previous QENS studies on proton conducting oxides have been performed by the use of time-of-flight and backscattering techniques, which give access to the time-scale of picoseconds, extended up to ≈1 ns in some cases, whereas even slower time-scales can be accessed with the NSE technique. Fig. 2 shows, as an example, approximate $(Q,\hbar\omega)$ domains as covered by the various spectrometers at the ILL. Included in the figure are the $(Q,\hbar\omega)$ ranges of relevance for diffusional dynamics in proton conducting oxides, as will be discussed further below.

A brief description of the various QENS techniques, emphasizing the essentials of each method, is presented in the following. A comprehensive description of the techniques can be found elsewhere. [11–13]

**2.4.1 Time-of-flight spectroscopy.** The typical energy resolution of time-of-flight spectrometers ranges between approximately 1 $\mu$eV and 1000 $\mu$eV, which implies that dynamics with characteristic time-scales faster than some hundreds of picoseconds usually can be investigated, *cf.* Fig. 2. These spectrometers can be designed to operate either in (i) direct-geometry or (ii) indirect-geometry mode. Direct-geometry spectrometers work with a pulsed monochromatic neutron beam impinging on the sample. The monochromator usually consists of a system of rotating disc choppers, which selects neutrons with a specific velocity out of an incoming broad distribution of neutron velocities as defined by the neutron moderator. The chopper system also serves to pulse the neutron beam in time. The final energy is determined by the time-of-flight between the sample and detector. In this way the distribution of scattered neutron velocities (energies) can be determined. In indirect-geometry spectrometers, on the contrary, a specific energy of the scattered neutrons is detected. In practice, this means using a *quasi-white* beam which is il-

† The activation of Raman scattering relies on changes in polarizability of the vibrating moieties. In INS, all modes are *active* and in principle measurable.

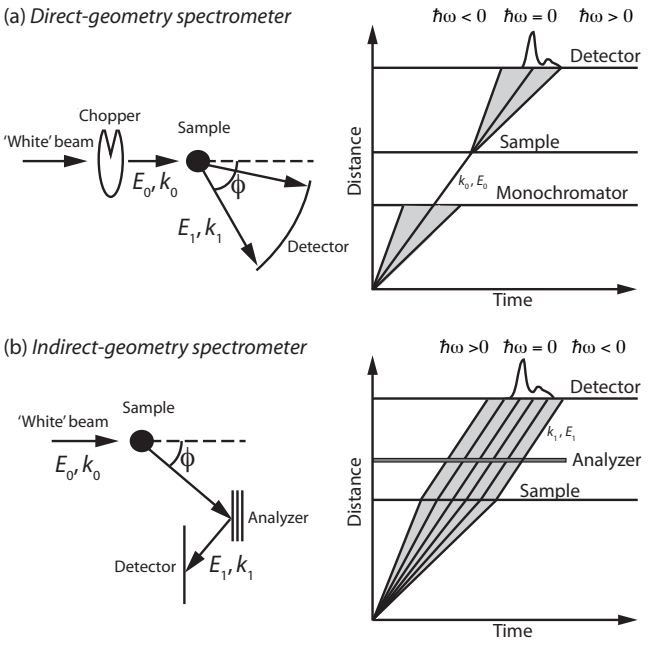


**Fig. 3** Schematic illustrations of direct-geometry (a) and indirect-geometry (b) spectrometers, together with their corresponding distance-time diagrams for single pulses of neutrons.

luminating the sample and analyzing the wavelength of the scattered neutrons by Bragg diffraction from a monocrystal. By differentiating Bragg's law, it can be shown that the energy resolution for these inverted-geometry spectrometers is given by

$$\Delta E/E = 2\Delta\lambda/\lambda = 2\sqrt{(\cot\theta\cdot\Delta\theta)^2 + (\Delta d/d)^2}, \qquad (12)$$

where $\theta$ is the Bragg angle and $d$ the lattice parameter of the monocrystal analyzer. As the lattice parameter can be determined with very high precision (typically, $\Delta d/d \approx 10^{-4}$), the latter term can be ignored and instead the dominant term is $\cot\theta\cdot\Delta\theta$. It follows that the highest energy resolution is achieved when the Bragg angle approaches 90°, since then $\cot\theta$ tends to zero, and therefore these spectrometers are also called backscattering spectrometers. In Fig. 3 is shown schematic illustrations of the major components of the two types of instruments. An overview of the beam trajectories by means of distance-time diagrams are also shown.

When planning an experiment on a time-of-flight spectrometer, the interplay of instrumental energy resolution and signal intensity is an important concern. Generally, the resolution increases with the use of longer neutron wavelengths, however the intensity is then usually decreased; for instruments on guide tubes the intensity varies as $\lambda^{-3}$ at long wavelengths. A further disadvantage of increasing the neutron wavelength is

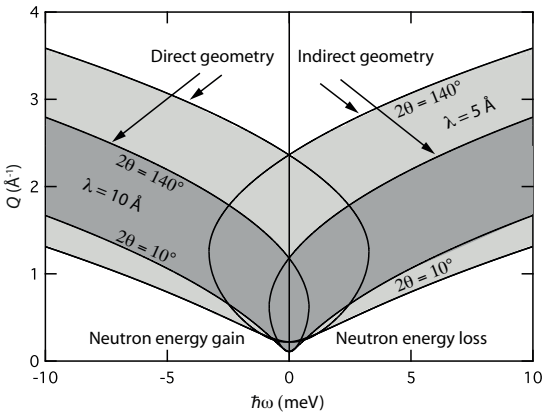


**Fig. 4** Plots of the accessible region in ($Q$,$\hbar\omega$) space for direct-geometry and indirect-geometry spectrometers, with neutrons of wavelength 5 and 10 Å (energy 3.272 and 0.818 meV, respectively). The minimum and maximum scattering angles are 10° and 140°.

that the accessible region in ($Q$,$\hbar\omega$) space gets reduced. This is determined by the laws of conservation of energy and momentum in the scattering process [Eq. (4-5)] and depends on the particular values of neutron energy and scattering angle. For a direct-geometry spectrometer, it follows that the accessible region is limited by

$$\hbar^2Q^2/2m = 2E_0 - \hbar\omega - 2\sqrt{E_0(E_0-\hbar\omega)}\cos 2\theta, \qquad (13)$$

whereas for an indirect-geometry spectrometer, the accessible region is limited by

$$\hbar^2Q^2/2m = 2E_1 + \hbar\omega - 2\sqrt{E_1(E_1+\hbar\omega)}\cos 2\theta. \qquad (14)$$

Fig. 4 shows the accessible regions for the two types of spectrometers and two choices of neutron energy. Note that for fixed incident energy (as in direct-geometry spectrometers) and for fixed analyzed energy (as in indirect-geometry spectrometers), the curves that define the measurable ($Q$,$\hbar\omega$) region are identical in shape but are each other's mirror image. Furthermore, one should note that direct-geometry spectrometers cannot measure neutron energy losses that are larger than the value of the incident neutron energy, since the final neutron energy can never be less than zero. Similarly, inverted-geometry spectrometers cannot measure neutron energy gains larger than the value of the neutron energy measured by the analyzer. Examples of currently operational time-of-flight spectrometers include: IN4 (ILL), IN5 (ILL), IN6 (ILL), TOFTOF (FRM-II), FOCUS (PSI), MAPS (ISIS), MARI (ISIS), MERLIN (ISIS), LET (ISIS), DCS (NCNR), ARCS (SNS), CNCS (SNS), SEQUOIA (SNS), PELICAN (OPAL), and HRC and AMATERAS (J-PARC).

**2.4.2 Backscattering spectroscopy.** Whereas time-of-flight spectrometers utilize either direct- or indirect-scattering

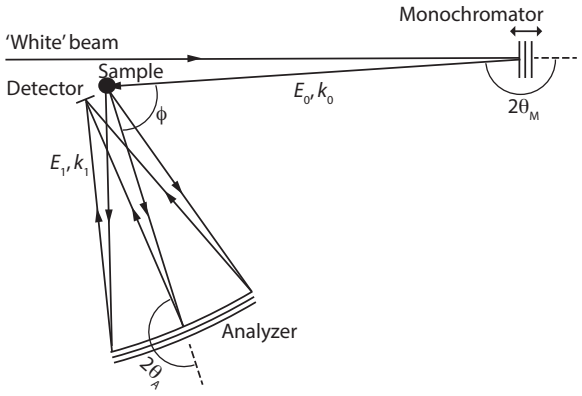


**Fig. 5** Schematic illustration of a backscattering spectrometer based on Doppler broadening.

geometry, the technique known as backscattering is the limiting case of the latter. Specifically, it has the energy analyzer positioned in perfect or near backscattering geometry ($\theta_A \approx 90^\circ$), in addition it utilizes a monochromator, also that in perfect or near backscattering geometry ($\theta_M \approx 90^\circ$), before the sample, *cf.* Fig. 5. Using the same argument as for the "conventional" indirect-geometry time-of-flight spectrometers, the backscattering geometry increases the energy resolution according to Eq. (12). Furthermore, as both the monochromator and analyzer are set in backscattering geometry, the energy transfer is fixed. This means that if one wants to achieve a dynamical range of say 10 times the resolution, the energy of the incoming neutrons has to change by the same amount. The manner in which this is done is by giving the monochromator a translational motion (Doppler broadening),[14] or by thermal expansion of the lattice parameters of the monochromator crystal.[15] The former approach requires much shorter measuring times and is usually adopted. However, the latter one yields a much larger dynamical range not limited by the speed of the Doppler driven monochromator.

Backscattering spectrometers are characterized by a higher energy resolution than time-of-flight spectrometers. Typical energy resolutions are between 0.3 $\mu$eV and 1 $\mu$eV. This translates into the time-scale of nanoseconds, that is much slower than the time-scales probed by most time-of-flight spectrometers. Although most backscattering spectrometers have been built on neutron research reactors and use a monocrystal monochromator, backscattering spectrometers built on spallation sources do not use such monochromators, but instead the incident neutron energy is determined from the overall time-of-flight between the neutron source and the detectors. A dynamical range of several hundred $\mu$eV is achievable. Currently operational backscattering spectrometers include: IN10 (ILL), IN13 (ILL), IN16B (ILL), SPHERES (FRM-II), IRIS (ISIS), OSIRIS (ISIS), HFBS (NCNR), and BASIS (SNS).

**2.4.3 Spin-echo spectroscopy.** As described above, time-of-flight and backscattering spectrometers rely on the determination of the exchange in neutron energy *via* the measurements of time-of-flight before and after the scattering event, respectively, or by monochromization by monocrystals. The smaller the energy exchange is, the more precise the neutron speed has to be defined. This can be achieved only at the expense of infinitely low count rate and sets a practical resolution limit of 0.1–1 $\mu$eV for these types of instruments. In NSE spectroscopy, on the other hand, the energy resolution is decoupled from the neutron intensity and as a consequence it is possible to measure the energy exchange of each individual neutron in the scattering event irrespective of their energy.[16–18] Currently available NSE instruments achieve energy resolutions of the order of 0.1 neV to 1 neV, which in terms of measurable time-scales translate into the regime of picoseconds to hundreds of nanoseconds, thus allowing studies of relatively slow diffusional processes but, importantly, still on an atomic length-scale. In addition, NSE covers a very wide time-range, of several decades, often with the same instrumental setting.[16–18] It follows that NSE spectroscopy offers unique opportunities to obtain information about dynamical processes occurring on significantly different time-scales in the same measurement.

The basic principle of NSE is as follows. First, neutrons from a cold moderator are monochromized with the use of a neutron velocity selector, which gives a relatively wide range of neutron wavelengths ($\Delta\lambda/\lambda \approx 15\%$ FWHM). These neutrons are then polarized along their velocity direction ($x$), before their spins are rotated to a direction perpendicular to the velocity direction ($z$) by the use of a $\pi/2$ spin flipper, see Fig. 6(a). Then, the neutrons travel in the first precession coil through a magnetic field aligned along the $x$ direction. Here, the neutrons undergo a specific number of Larmor precessions in the $yz$ plane, determined by the neutron velocity ($v$), length of the coil ($L$), and magnetic field strength ($B$). Accordingly, the total precession angle (in radians) over the length of the first solenoid can be expressed as

$$\varphi_1 = \frac{\gamma BL}{v}, \tag{15}$$

where $\gamma$ is the neutron gyromagnetic ratio. For a typical flux density line integral $BL$ (or more strictly $\int^L \boldsymbol{B}d\boldsymbol{l}$) of 0.3 Tm, the polarization of 10 Å neutrons will undergo more than 20 000 precessions. It is clear that the relatively wide range of neutron wavelengths is rapidly dephased and the final net polarization at the end of the first solenoid will be zero. Before the neutrons are scattered by the sample, the neutron spins are rotated by 180 degrees around the $z$ axis by a $\pi$ spin flipper. After the scattering event, the neutrons travel through the second solenoid, which is identical to the first one, with the con-

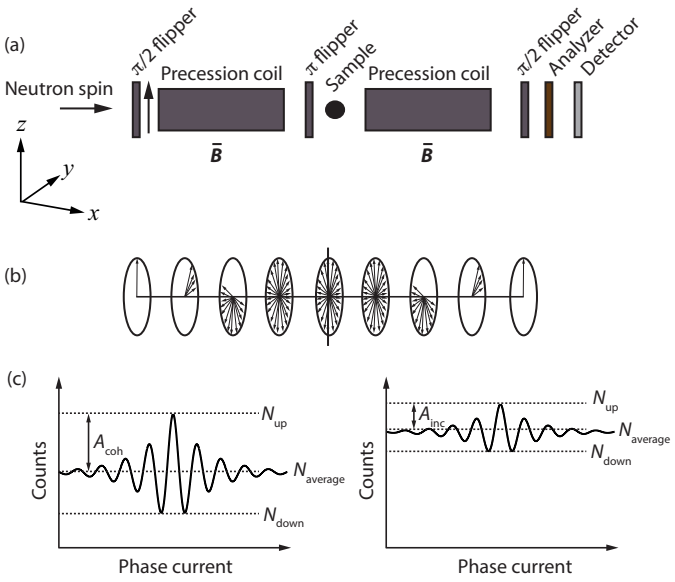


**Fig. 6** (a) The layout of a generic spin-echo spectrometer showing its principal components. (b) Schematic representation of the dephasing of the precessing neutron spins along the first arm of the spectrometer, followed by a $\pi$ spin flip and subsequent rephasing along the second arm. (c) NSE signal, for a fixed $Q$-value, as a function of the phase difference between the incident and scattered beams, in the case of purely coherent and incoherent scattering, respectively. $A_{\rm coh}$ and $A_{\rm inc}$ are the echo amplitudes for coherent and incoherent scattering, $N_{\rm average}$ is the average count rate outside the echo, and $N_{\rm up}$ and $N_{\rm down}$ are the count rates of non-spin-flip ($\pi$ flipper off) and spin-flip ($\pi$ flipper on) measurements made with the $\pi/2$ flippers off.

sequence being that the neutrons now precess in the opposite direction.

If the scattering is purely elastic, the neutron spin direction at the end of the second coil will equal that at the beginning of the first coil and the total precession angle is then zero, $\varphi = \varphi_1\text{-}\varphi_2 = 0$, irrespective of the spread of neutron velocities, see Fig. 6(b). The final neutron polarization is measured by flipping the neutron spins back into the longitudinal $x$-direction using a $\pi/2$-flipper and finally analyzing it with an array of supermirrors in front of the detector that transmits only neutrons of one polarization direction. Since the angle between the neutron polarization and the analyzer direction is $\varphi$, then the probability that a neutron is transmitted is $\cos(\varphi)$. What is measured experimentally is the expectation value (average) over all the scattered neutrons, *i.e.* $\langle\cos(\varphi)\rangle$.

If the scattering is quasielastic, the situation is different since the energy and hence the velocities of the neutrons will change at the scattering event, and the neutrons' spins will therefore not return to their initial state. Accordingly, the accumulated precession angle will be

$$\varphi = \gamma BL\left(\frac{1}{v_1} - \frac{1}{v_2}\right), \tag{16}$$

where $v_1$ and $v_2$ are the velocities of the incident and scattered neutrons, respectively. Expressing the energy transfer in terms of $\hbar\omega = m/2(v_2^2\text{-}v_1^2)$, it can be shown that the accumulated precession angle with respect to the echo condition is

$$\varphi = \frac{\hbar\gamma BL}{mv_1^3}\omega = t\omega. \tag{17}$$

The proportionality constant $t = \hbar\gamma BL/mv_1^3$ has the units of time and is called the *spin-echo* or *Fourier time*. Noting that at a given $Q$, the probability for scattering with an energy exchange $\hbar\omega$ is by definition $S(Q,\hbar\omega)$, thus the final beam polarization measured at the echo position (where the field integrals in the first and second arm are exactly matched) is‡

$$P_x = \langle\cos(t\omega)\rangle \propto \int \cos(t\omega)S(Q,\omega)d\omega. \tag{18}$$

This is nothing else than the Fourier transform of $S(Q,\omega)$ with respect to $\omega$. Thus, the measurement of the final beam polarization for a given *Fourier time*, $t$, is simply a measurement of the intermediate scattering function, $I(Q,t)$.

$$P_x = \langle\cos(t\omega)\rangle \propto I(Q,t). \tag{19}$$

In other words, data is recorded as a function of real time, and not as a function of energy transfer as in the case of time-of-flight and backscattering spectroscopy. Different *Fourier times* are measured by varying the field integral (by the precession field of the first coil) around the symmetry point between the two coils. This will give an echo group as a function of phase current [Fig 6(c)], where the periodicity of the damped oscillation is determined by the average wavelength and its envelope is the Fourier transform of the wavelength distribution.

As in all types of neutron scattering experiments, the $I(Q,t)$ can be divided into coherent and incoherent parts, $I(Q,t) = I_{\rm coh}(Q,t) + I_{\rm inc}(Q,t)$. Incoherent scattering is featured by a 2/3 probability of flipping the spins of the neutrons, effectively reducing the incoherent NSE signal by 2/3, and, in addition, contributing to a background [Fig 6(c)].[19] Hence, the intermediate scattering function measured by NSE can be expressed as

$$I_{\rm NSE}(Q,t) = I_{\rm coh}(Q,t) - \frac{1}{3}I_{\rm inc}(Q,t). \tag{20}$$

Generally, NSE provides the normalized intermediate scattering function obtained as

$$\frac{I_{\rm NSE}(Q,t)}{I_{\rm NSE}(Q,t=0)} = \frac{2A}{N_{up} - N_{down}}, \tag{21}$$

‡ The proportionality constant originates from instrumental factors which can be accounted for.

where $A$ is the echo amplitude and $N_{up}$ and $N_{down}$ are the maximal and minimal count rates, respectively. These are usually determined by performing measurements with the $\pi$ flipper on and off, respectively, while having the $\pi/2$ flippers off. It implies that the instrument is setup in such a way that the neutrons' spins and the magnetic fields are aligned parallel effectively zeroing the precession. The amplitudes of coherent and incoherent scattering, $I_{\rm coh}(Q,t=0) = S_{\rm coh}(Q)$ and $I_{\rm inc}(Q,t=0) = S_{\rm inc}(Q)$, respectively, can also be determined by measuring the intensities of spin-flip and non-spin flip scattering.

As it has been highlighted before, a wealth of information is obtained by analyzing the $Q$-dependence of the QENS component. Whereas time-of-flight and backscattering instruments allow the collection of data in the whole accessible range of $Q$-values in ones, NSE spectrometers, generally, collect data from a limited range of $Q$-values for each configuration. This is a big hindrance for all NSE experiments in which the signal of interest is not concentrated in a limited $Q$-range. The availability of a detector covering 30° of scattering angle on IN11-C at the ILL, partially overcome this disadvantage, although at the expense of a limitation in the maximum Fourier time achieved. The WASP instrument, which is currently being built at the ILL and which will allow to collect data over even larger scattering angle ranges should allow in the future for a much more efficient data collection in many chemical physics experiments, including investigations of proton conduction. Currently operational NSE spectrometers include: IN11 and IN11-C (ILL), IN15 (ILL), J-NSE and RESEDA (FRM-II), NSE (NCNR), NSE (SNS) and MUSES (LLB).

## 3 QENS on proton conducting oxides

QENS has played a central role in the field of proton conducting oxides and provided important information about the dynamics of protons in this class of technologically important materials. The usefulness of QENS for studies of proton conducting oxides comes from the fact that it gives access to the relevant time- and length-scales on which the atomic-scale dynamics of protons occur. In addition, the very large incoherent neutron scattering cross section of protons of 80.26 barns (1 barn = $10^{-24}$ cm$^{-1}$), far larger than all other nuclei (< 10 barns), and relatively small coherent scattering cross section (1.76 barns), enables one to observe protons essentially free from constructive interference, *i.e.* information about proton self-diffusion can be obtained, whereas the correlation between the dynamical behavior of an ensemble of protons can be neglected.§ Furthermore, the strong scattering signal from protons provides a good contrast in experiments and enables studies of proton self-diffusion in systems containing only relatively small amounts of protons. It follows that the total dynamical structure factor, $S(Q,\omega)$, can, in most cases, be approximated with the incoherent dynamical structure factor, *i.e.* $S(Q,\omega) \approx S_{\rm inc}(Q,\omega)$. The measured structure factor is a convolution of $S_{\rm inc}(Q,\omega)$ and the resolution function of the instrument, $R(Q,\omega)$, that is

$$S_{\rm meas}(Q,\omega) = S_{\rm inc}(Q,\omega) \otimes R(Q,\omega). \quad (22)$$

The resolution function is usually determined by a measurement of the sample at very low temperature (<10 K), where the diffusional dynamics is *frozen-in*, or on a 'perfectly' elastic, incoherent, scatterer, such as vanadium, of the same geometry as the sample.

When the QENS is accompanied by an elastic component, which is the case for localized motions, the dynamical structure factor may be expressed as

$$S_{\rm inc}(Q,\omega) = e^{-\langle u^2\rangle Q^2}\left\{ S^{\rm el}_{\rm inc}(Q)\delta(\omega) + S^{\rm inel}_{\rm inc}(Q,\omega)\right\}. \quad (23)$$

Here, the exponential factor is known as the Debye-Waller factor, which accounts for the decrease in elastic and quasielastic intensity due to vibrational motions of atoms (*i.e.* inelastic scattering). $\langle u^2\rangle$ is the total mean square displacement of all atoms due to vibrational motions in the material. $S^{\rm el}_{\rm inc}(Q)\delta(\omega)$ and $S^{\rm inel}_{\rm inc}(Q)$ represent the elastic and quasielastic contributions, respectively. Studying their dependence on $Q$ and temperature will bring a wealth of information, such as the timescale and geometry of the diffusive process(es) in the system under investigation.

### 3.1 Diffusion models

Theoretical models are based on the van Hove correlation function formalism and they predict the profile of $S(Q,\omega)$ and $I(Q,t)$, according to the kind of dynamics in the system. Generally, the quasielastic part of $S(Q,\omega)$ can be described by one or more Lorenzian functions, related to one or more dynamical processes, *i.e.*

$$S^{\rm inel}_{\rm inc}(Q,\omega) = \sum_{l=1} A_l(Q) L_l(Q,\omega), \quad (24)$$

where the Lorentzian function is

$$L_l(Q,\omega) = \frac{1}{\pi}\frac{\Gamma(Q)_l}{(\hbar\omega)^2 + \Gamma(Q)_l^2}. \quad (25)$$

and $\Gamma(Q)_l$ is its half-width at half-maximum (HWHM). Here, the $Q$-dependence of the latter provides information about the geometry of the dynamics and hence adds a useful mean to distinguish between different models. For random (Brownian)

§ For a complete list of the thermal neutron scattering cross sections of all elements and its isotopes, the reader is referred to ref. [20].

translational diffusion, $\Gamma(Q)$ follows a parabolic increase with increasing $Q$, *i.e.*

$$\Gamma(Q) = 2\hbar D_s Q^2, \tag{26}$$

where $D_s$ is the self-diffusion coefficient. $D_s$ relates to the relaxation time $\tau$ according to

$$\tau = \frac{1}{2D_s Q^2}. \tag{27}$$

Random translation diffusion, also known as continuous diffusion, is, however, only observed at small $Q$-values, which correspond to large distances in real space. At larger $Q$-values, the motion is no more continuous and underlaying microscopic mechanisms are at play. To describe such mechanistic detail, several types of jump-diffusion models have been developed. These all describe long-range diffusion as a series of successive jumps and contain as parameters the characteristic jump length and time between successive jumps (the latter is referred to as residence or relaxation time). One of the most used models is that developed by Chudley and Elliott,[21] which assumes a constant jump length, $r$, a residence time, $\tau$, and a negligible jump time, At sufficiently small $Q$-values, the $\Gamma(Q)$ still follows a $Q^2$-behavior, as in the case for continuous diffusion, but at larger $Q$-values $\Gamma(Q)$ follows an oscillatory behavior according to

$$\Gamma(Q)_{C-E} = \frac{\hbar}{\tau}\left(1 - \frac{\sin(Qr)}{Qr}\right). \tag{28}$$

Related jump-diffusion models are the Hall-Ross model,[22] which is characterized by a Gaussian distribution of jump lengths, and the Singwi-Sjölander model,[23] which is characterized by an exponential distribution of jump lengths. However, one should note that diffusion processes are often more complicated and cannot always be categorized into these relatively simple cases, hence more sophisticated models must be developed. A detailed description and survey of different models can be found in several text books or review articles, see *e.g.* refs.[12,24]

## 4 Overview of QENS studies

This section reviews the literature on QENS studies on proton conducting oxides. The aim is not to give an exhaustive account for all the work that has been done in this field, but to illustrate different uses of QENS and to summarize some of the key results obtained so far. This is followed by my critical remarks as well as a discussion about the prospectives for future studies in this area of research.

### 4.1 Perovskite structured oxides

The majority of previous QENS studies on proton conducting oxides have been performed using time-of-flight and backscattering methods and on perovskite structured materials, such as doped variants of $BaZrO_3$ and $BaCeO_3$ based compounds; these studies are here summarized briefly. The initial studies were performed by Hempelmann *et al.*[25] and Matzke *et al.*[26] in the mid nineties on a hydrated sample of $SrCe_{0.95}Yb_{0.05}O_{2.975}$. Fig. 7 shows the QENS spectra measured at different temperatures. From the low-$Q$ data, it was possible to extract the proton self-diffusion constant as a function of temperature and this was found to be comparable to the bulk proton conductivity measured with impedance spectroscopy.[25] The high-$Q$ data was also analyzed and this contains information about the mechanistic detail of the proton conduction. Analysis showed that the QENS spectra could be reproduced by two quasielastic components, corresponding to two different localized proton motions with different activation energies, suggesting the existence of two different proton sites occupied by the protons. More detailed analysis showed that the QENS data was in agreement with a two-state model superimposed of the Chudley-Elliott model. The Chudley-Elliott model suggests in this case that the proton conduction occurs as a series of proton jumps (transfers) between neighboring oxygens, O(1) and O(2), and rotational diffusion of the -OH group between such transfers, see Fig. 8(a), whereas the two-state model indicates that the proton diffusion consists of some sort of trapping and release events.

The O(1)–H···O(2) transfer direction may be modeled by a double Morse type potential, with a barrier height dependent on the separation distance between O(1) and O(2) and on the vibrational level of the O-H stretch mode, which is illustrated

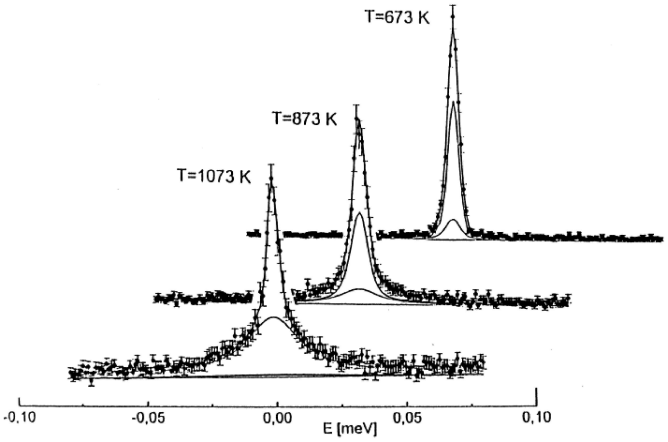


**Fig. 7** Neutron scattering spectra, $S(Q,\omega)$ of $SrCe_{0.95}Yb_{0.05}H_{0.02}O_{2.985}$ for different temperatures at momentum transfer $Q = 0.29$ Å$^{-1}$. The solid lines show the total scattering function as well as the two components of the two-state model. Reprinted with permission from ref.[25], copyright Elsevier, 1995.

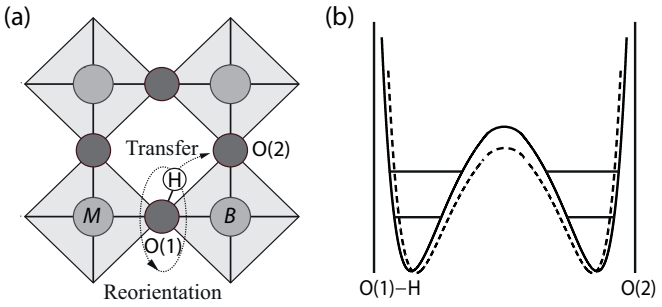


**Fig. 8** (a) Schematic of the elementary local dynamical processes in the proton conduction mechanism in a $AB_{1-x}M_xO_3H_x$ type perovskite with cubic symmetry, where $M$ is the acceptor dopant. (b) The proton occupies a double Morse type potential with barrier height dependent on the separation distance between neighboring oxygens, O(1)–O(2). The horizontal lines depict vibrational energy levels for the O-H stretch mode. The dashed curve indicates the change in potential energy due to phonons of the perovskite host lattice.

in Fig. 8(b). Thus, the rate of proton diffusion is believed to be strongly coupled to the vibrational dynamics of the system. In particular, the proton performs localized O-H stretch and wag modes, which may be seen as precursors to the transfer and reorientational step, respectively, and moreover the dynamics of the oxygen sub-lattice induce large fluctuations in the distances between O(1) and O(2) with time.[27,28]

Such a proton conduction mechanism in perovskites has later found support from several computer simulations and experiments on different proton conducting oxide systems ever since. In particular, muon spin-relaxation experiments[29] and several simulations[30–33] have indicated that the dopant atoms are responsible for the trapping effect in these materials, thus decreasing the overall proton conductivity. Simulations have for example reproduced the experimental trend in proton conductivity in the $BaZr_{0.9}M_{0.1}O_{2.95}$ ($M$ = Y, In, Sc and Ga) series for which the conductivity differs several orders of magnitude depending on the type of dopant atom.[34] More recently, the trapping view was further supported by combined thermogravimetric and a.c. impedance spectroscopy data on $BaZr_{0.8}Y_{0.2}O_3H_{0.2}$.[35] However, converse to the view that dopant atoms act as localized trapping centers for the proton diffusion, it has also been proposed that the dopant atoms may affect the proton transport in a more nonlocal manner.[36,37]

Following the pioneering work by Hempelmann *et al.*[25] and Matzke *et al.*[26], Karmonik *et al.*[38] investigated the proton dynamics in the double perovskite structured material $Ba[Ca_{0.39}Nb_{0.61}]O_{2.91}$ which, similarly to the previous studies on $SrCe_{0.95}Yb_{0.05}O_{2.975}$, gave support for a proton conduction mechanism divided into proton jumps and reorientational motions. Subsequently, Pionke *et al.*[39] reported on the proton self-diffusion constant for protons in the same material. Later, Groß *et al.*[40] and Beck *et al.*[41] investigated the influence of particle size on the atomic-scale proton diffusion in $BaZr_{0.85}M_{0.15}O_{2.925}$ ($M$ = Y, In, and Ga). A key result is that only the microcrystalline samples showed a clear quasielastic signal related to proton motions. It was imagined that in the nanocrystalline samples, the protons are concerted mainly to the GB regions or to the surface of the crystallites. More recently, Wilmer *et al.*[42] investigated the proton dynamics in $BaZr_{0.90}Y_{0.10}O_{2.95}$. Attempts to interpret the data in the framework of the two-state model yielded unconvincing results. A simpler approach using the isotropic Chudley-Elliott model yielded reasonable values for the proton self-diffusivities but also unusually high values for the jump distance which was found to be close to the mean distance between dopants of approximately 9 Å. Furthermore, Malikova *et al.*[43] performed a simultaneous structural and dynamic study on $BaCe_{0.90}Y_{0.10}O_{2.95}$, by combining neutron diffraction with QENS. A key result was that the dehydration occurs over a large temperature range (from 500 °C to 800 °C), providing evidence for the presence of proton sites with a variable degree of hydrogen bonding strengths to the perovskite lattice. Slodczyk *et al.*[44] investigated proton dynamics in Yb-doped $BaZrO_3$, and they observed the onset of proton diffusion at a temperature of approximately 600 °C, whilst Karlsson *et al.*[45] reported on a QENS study of $BaZr_{0.90}M_{0.10}O_{2.95}$ ($M$ = Y and Sc). In the latter study, the authors revealed a localized proton motion on the ps timescale and with a small activation energy of 10–30 meV, for both materials. Comparison of the QENS results to density functional theory calculations suggests that for both materials this motion may be ascribed to intra-octahedral proton transfers occurring close to a dopant atom. Braun *et al.*[46] reported on the Y-doped material, $BaZr_{0.90}Y_{0.10}O_{2.95}$, and found two different activation energies for proton diffusion at different ranges of temperature. Colomban *et al.*[47] reported on a change in local proton dynamics across a structural phase transition in $(Ba/Sr)Zr_{1-x}Ln_xO_{3-\delta}$, whilst Slodczyk *et al.*[48] investigated proton dynamics in $SrZr_{0.90}Yb_{0.10}O_{2.95}$ and $BaZr_{0.90}Yb_{0.10}O_{2.95}$. Measurements taken in the temperature range from 400 °C to 700 °C showed on a peak in the mean square displacement of the protons at around 500 °C, suggesting a maximum in proton diffusivity around this temperature. Most recently, Chen *et al.*[49] measured simultaneously macroscopic proton conductivity and atomic-scale proton diffusivity in $BaCe_{0.8}Y_{0.2}O_{2.9}$, by means of an *in-situ* impedance spectroscopy cell in combination with the QENS measurements. A key result was that the QENS data could be interpreted in terms of inter-octahedral proton transfer.

Whereas all the above mentioned work was done with the

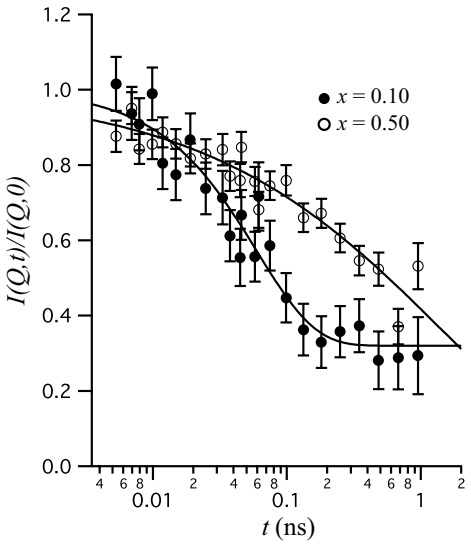


**Fig. 9** $I(Q,t)/I(Q,0)$ of $BaZr_{1-x}In_xO_{3-x/2}$ ($x = 0.10$ and 0.50) at 500 K and $Q = 1.05$ Å$^{-1}$. The lines represent fits with a single exponential plus a constant ($x = 0.10$) and a KWW stretched exponential function ($x = 0.50$), respectively. Reprinted with permission from ref.[51], copyright American Chemical Society, 2010.

use of time-of-flight and backscattering methods, there are only three reports[50–52] on the use of NSE spectroscopy for studies on proton conducting oxides, despite its unique benefits. The initial work was done by Karlsson *et al.*[50] on a hydrated sample of $BaZr_{0.90}Y_{0.10}O_{2.95}$. A key result was that the protonic self-diffusion constant, measured over a length scale of 5–8 unit cell lengths, is comparable with that as extracted from conductivity experiments. This suggests that already on a length-scale as short as ≈20 Å the effect of potential local traps or other "imperfections" in the structure that can be expected to affect the proton dynamics, has averaged out. That is, there are no new features revealed on a larger length-scale that have not been experienced by the proton on the shorter length-scale probed by NSE.

More recently, Karlsson *et al.*[51] investigated the dopant concentration dependence of the local proton dynamics in $BaZr_{1-x}In_xO_{3-x/2}$ ($x = 0.10$ and 0.50). Fig. 9 shows the normalized intermediate scattering function, $I(Q,t)/I(Q,0)$, for the two materials at 500 K and $Q = 1.05$ Å$^{-1}$. The relaxational decay with increasing Fourier time relates to dynamics of the protons. A key result is that the shape of the $I(Q,t)/I(Q,0)$s differ significantly for the two materials. For $x = 0.10$, the $I(Q,t)/I(Q,0)$ is reflected by a single exponential decay and a constant, $I(Q,t)/I(Q,0) = [1\text{-}c(Q)]e^{-t/\tau(Q)} + c(Q)$, where $\tau = 60$ ps is interpreted as the characteristic relaxation time for a localized proton motion, whereas the plateau at long time-scales ($c = 0.32$) relates to the scattering from protons that are essentially immobile within the experimental NSE time-window. For $x = 0.50$, on the other hand, the $I(Q,t)/I(Q,0)$ is stretched in time and fits much better to a Kohlrausch-Williams-Watts (KWW) stretched exponential function,[53,54] $I(Q,t)I(Q,0) = e^{-[t/\tau_{KWW}(Q)]^{\beta(Q)}}$ where $\tau_{KWW}(Q)$≈4 ns is a characteristic time of a relaxational process and $\beta(Q)$≈0.42 is the, so called, stretching parameter. The authors interpreted the stretched relaxational decay in terms of a large distribution of diffusional rates for the protons as due to many different local structural environments around the protons in the material. This is physically reasonable since the high concentration of In is known to induce strong short-range structural perturbations of the longer-range, average, cubic perovskite structure. The structural distortions become more and more pronounced with increasing dopant level and it has been suggested that they are related to tilting of the $(In/Zr)O_6$ octahedra due to the size difference between the $In^{3+}$ and $Zr^{4+}$ ions.[55] Further, it has been suggested that there is a compositional "threshold" between $x = 0.10$ and 0.25 above which the dopant induced structural distortions distribute throughout the entire perovskite structure, although with no long-range coherence in terms of the length-scales typically probed by diffraction.[55] Thus, the more well-defined time-scale of the proton motion observed for $x = 0.10$ is likely to results from the more ordered local structure of the material. Interestingly, the idea of a compositional "threshold" between $x = 0.10$ and $x = 0.25$, compares to a rise in conductivity from $2.9\cdot10^{-5}$ S/cm for $x = 0.10$ to $2.6\cdot10^{-4}$ S/cm for $x = 0.25$, which may indicate that some structural disorder is favorable for high proton conduction in perovskite type oxides.[55]

### 4.2 Novel structure types

Clearly, $ABO_3$-type perovskites continue to be the materials that are accumulating the largest interest within the solid state ionics community. However, there is a growing interest in alternative, more complicated, structure types and particularly in structure types containing tetrahedral moieties, such as lanthanum barium gallates, *i.e.* $LaBaGaO_4$-based compounds. The structure of $LaBaGaO_4$ consists of discrete $GaO_4$ tetrahedra, which are charge balanced by the Ba/La ions [Fig. 10(a)]. Increasing the Ba:La ratio results in the formation of oxygen vacancies, $La_{1-x}Ba_{1+x}GaO_{4-x/2}$, and similarly to perovskite type oxides such oxygen vacancies can be filled with hydroxyl groups during a hydration procedure. The presence of oxygen vacancies leads to considerable relaxation of neighboring $GaO_4$ tetrahedra, resulting in the formation of $Ga_2O_7$ units so that the Ga retains tetrahedral coordination, however the hydration can lead to the breaking up of such units.

Recently, Jalarvo *et al.*[52,56] investigated atomic-scale dynamics of protons in a hydrated sample of $La_{0.8}Ba_{1.2}GaO_{3.9}$, using neutron backscattering and NSE spectroscopy. The

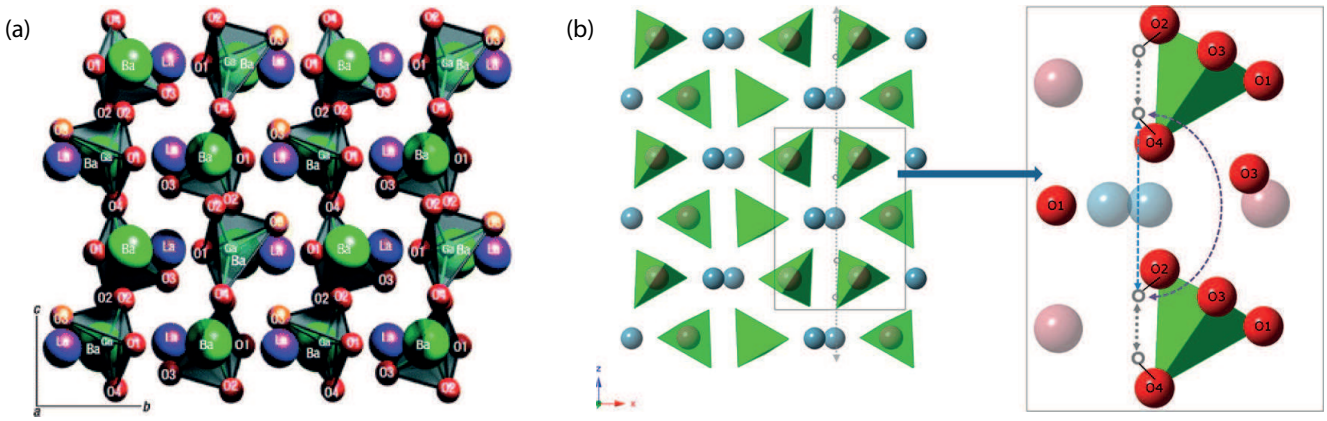


**Fig. 10** (a) Crystal structure of $LaBaGaO_4$, which is comprised of $GaO_4$ distorted tetrahedra and ordered alternating layers of lanthanum and barium ions. The $GaO_4$ tetrahedra are isolated from one another (with an elongated Ga–O3 bond). (b) Protons are represented as small grey-colored circles bound to particular corners of the $GaO_4$ tetrahedra. The proton migration takes place along the *c* axis, shown as a gray dashed arrow. The insert shows a slice parallel to the *ac* plane with the elementary steps: the intratetrahedron path is represented with gray arrows and two possibilities for intertetrahedra paths are represented with (i) blue and (ii) purple arrows. Reprinted with permission from ref.[52], copyright American Chemical Society, 2013.

backscattering spectra were fitted to two Lorentzian components; one narrow and one broader one, representing proton dynamics on different time-scales. The analysis of the narrow component showed that it can be related to continuous proton diffusion with an activation energy of 0.44 eV. This activation energy is somewhat smaller than that extracted from conductivity experiments (0.56 eV), but in perfect agreement with the activation energy for intratetrahedron proton jumps as determined by calculations that suggest this process to be rate-limiting for the longer-range proton diffusion.[56] The analysis of the broader component shows that this is related to localized proton motions with an activation energy of 0.068 eV, which is similar to the calculated intertetrahedra proton transfer value. On the basis of these results it was suggested that the proton conduction occurs as a series of intratetrahedron proton jumps between the O2 and O4 sites, and intertetrahedron proton jumps from O4 to O2 [*cf.* Fig. 10(b)]. The intertetrahedron proton jumps are suggested to take place either directly along the *c* axis, or *via* the O3 site of a neighboring $GaO_4$ tetrahedron, whereas the overall long-range proton transport takes place along the *c* axis. The proton conduction mechanism is thus so-called *Grotthuss*-like, which means that the protons diffuse stepwise throughout the structure of the material. Between each proton jump, the proton is covalently bound to an oxygen and performs O-H stretch and wag vibrational motions, superimposed of the vibrational dynamics of the oxygen lattice. These motions induce fluctuations in the distance between the proton and a neighboring oxygen to which the proton may jump, thus creating transient hydrogen bonds that affect strongly the probability for proton transfer.

## 5 Critical remarks and outlook

It has been shown that the majority of QENS studies has been performed on classic proton conducting perovskites, in particular on materials based on $BaZrO_3$ and $BaCeO_3$, whereas only a few studies have been performed on other structure types. Although, clearly, these studies have provided important information about the dynamical behavior of protons in oxides, several of them have suffered from either a weak scattering signal or from the limited $(Q,\omega)$ range as accessed with the variety of instruments that have been used. As a consequence, it has often been difficult or impossible to find models that reliably describe the data and therefore to draw any firm conclusions on what type of motions that were observed. Furthermore, there are, in some cases, disagreements between the results obtained in different studies, even when the same material was investigated. However, in view of the different types of instruments and instrumental settings that have been used, some reproducibility problems may be expected. In addition, the structural and physiochemical details of the investigated samples, as partly related to the details of the sample preparation, are of important concern.¶ In this context, the studies by Groß *et al.*[40] and Beck *et al.*[41] already highlighted the importance of particle size, hence synthesis route, on the atomic-scale proton diffusion in $BaZr_{0.85}M_{0.15}O_{2.925}$ ($M$ = Y, In, and Ga) proton conductors, but many more factors may be at play. Therefore, there is a need to perform systematic investigations, using the same experimental conditions and on

¶ This also accounts for the spread in proton conductivities for the same type of systems, as reported in the literature.[2]

well characterized samples, in order to be able to make good comparisons between different measurements. Such studies should include systematic investigations of the effect of type and concentration of dopant atoms, crystal structure, and level of hydration, on the atomic-scale proton dynamics, for example.

Although this article has highlighted the advantages of neutron scattering for research on proton conducting oxides, as with all techniques, QENS has its disadvantages. The primary drawback of QENS is that neutron scattering is an intensity-limited technique. In studies of proton conducting oxides, typically at least 10 grams of the sample is needed to obtain data of sufficient quality. These are very large samples for most other analytical techniques and obtaining a sufficient quantity can be problematic, particularly for new, complex, materials that may only be available in much smaller quantities. On the positive side, the large sample size does mean that concerns about representative sampling are much less severe than for techniques that operate on the milligram or smaller scale. Moreover, measuring times are at least a few hours per instrumental setting, thus kinetic measurements by QENS are generally not feasible. Any instrumental improvements with respect to advances in neutron flux and detector coverage, allowing faster acquisition times and smaller samples, in the form of single crystals or even thin films, to be investigated, are therefore highly welcome. For the future application of proton conducting oxides as fuel-cell electrolytes, one would indeed use a (thin) film of the proton conductor sandwiched between the anode and cathode materials. Other than in powder samples, such films can be highly textured and strained, which may affect significantly the proton conducting properties. Addressing diffusive processes in oxide films is however a lot more challenging than in bulk powder samples due to the heavily reduced sample volume. However, with the vision of the ESS, which, in comparison to present-day neutron sources, will offer considerably higher neutron flux, such experiments might become possible on a routine basis. Increasing the neutron flux may further open up for studies using polarization analysis, for the separation of coherent and incoherent scattering. Such analysis would not only distinguish between collective and self-dynamics but may also give information about proton-proton interactions, for example. Similar information may be obtained by the use of nuclear polarization methods, which offer exciting opportunity to tune continuously the spin-dependent scattering cross section of hydrogen nuclei and thereby the contrast between coherent and incoherent scattering.[57] Furthermore, there is a clear trend towards the developments of *in-situ* sample environments, which allow for at least one additional materials property to be measured simultaneously with the collection of the QENS spectra. In this way the inherent uncertainty that comes from correlating separate measurements can be avoided, or allow for measurements which today are not even feasible separately. We have already noted the recent study by Chen *et al.*[49], who combined QENS with impedance spectroscopy, thus allowing for the direct correlation between proton dynamics on significantly different time- and length-scales. Future work in this direction is likely to expand and will include the development and subsequent use of *in-situ* electrochemical cells, which allow for measurements under conditions that mimic those under fuel cell operating conditions.

## 6 Conclusions

To conclude, QENS is an important technique in the field of proton conducting oxides and has already contributed greatly to the understanding of proton dynamics in these materials, nevertheless the technique shows great potential for advancing further this understanding. Future work in this area is likely to comprise systematic investigations of well-characterized samples of both classic proton conducting perovskites as well as of new compounds and will take great advantage of the upgrade of existing neutron spectrometers and from the development of new instrumentation along with the construction of next-generation neutron sources. A better understanding of the mechanism of proton conduction in a wider family of oxide proton conductors is seen as crucial for the development of strategies for developing new materials with higher proton conductivity. This is in turn critical to future breakthroughs in the development of next-generation devices based on proton conducting oxides, such as intermediate-temperature fuel cells, hydrogen sensors, or other electrochemical devices. Even small or gradual advancements of the current understanding of proton conduction mechanisms in oxides may therefore be of considerable environmental and economic impact.

## Acknowledgments

Financial support from the Swedish Research Council (grant nr. 2010-3519 and 2011-4887) is gratefully acknowledged. Finally, many thanks to Antonio Faraone at the NIST Centre for Neutron Research for time and discussions and for valuable comments on the writing of this article.

## References

1 B. C. H. Steele and A. Heinzel, *Nature*, 2001, **414**, 345–352.
2 K. D. Kreuer, *Annu. Rev. Mater. Res.*, 2003, **33**, 333–359.
3 L. Malavasi, C. A. J. Fisher and M. S. Islam, *Chem. Soc. Rev.*, 2010, **39**, 4370.

4 P. J. Gelling and H. J. M. Bouwmeester, *Catalysis Today*, 1992, **12**, 1–105.

5 F. A. Kröger and H. J. Vink, *Solid State Physics: Advances in Research and Applications*, Academic Press, 1956.

6 C. T. Chen, C. E. Danel and S. Kim, *J. Mater. Chem.*, 2011, **21**, 5435.

7 M. Shirpour, R. Merkle, C. T. Lin and J. Maier, *Phys. Chem. Chem. Phys.*, 2012, **14**, 730.

8 I. M. Sosnowska, *Solid State Ion.*, 1999, **119**, 261–268.

9 M. Karlsson, *Dalton Trans.*, 2013, **42**, 317–329.

10 H. Jobic and D. N. Theodorou, *Micropor. Mesopor. Mat.*, 2007, **102**, 21.

11 T. Springer, *Quasielastic Neutron Scattering for the Investigation of Diffusive Motions in Solids and Liquids*, Springer-Verlag Berlin, Heidelberg, New York, 1972.

12 M. Bée, *Quasielastic Neutron Scattering*, IOP Publishing, Bristol, D.J. Millen ed., 1988.

13 L. Liang, R. Rinaldi and H. Schober, *Neutron Applications in Earth, Energy and Environmental Sciences*, Springer Science+Business Media, Heidelberg, New York, 2009, ch. 3.

14 M. Birr, A. Heidemann and B. Alefeld, *Nucl. Instr. and Meth.*, 1971, **95**, 435.

15 J. C. Cook, W. Petry, A. Heidemann and J.-F. Barthelemy, *Nucl. Instrum. Methods Phys. Res. A*, 1992, **312**, 553.

16 F. Mezei, *Zeitschrift fur Physik*, 1972, **255**, 146–160.

17 F. Mezei, *Neutron Spin Echo: Lecture Notes in Physics*, Springer, Heidelberg, 1980, vol. 28.

18 F. Mezei, C. Pappas and T. Gutberlet, *Neutron Spin Echo Spectroscopy: Basics, Trends and Applications*, Springer, 2003.

19 B. Farago, *Neutron Data Booklet*, Institut Laue-Langevin, Grenoble, France, 2002, ch. 2.8.

20 V. F. Sears, *Neutron News*, 1992, **3**,.

21 C. T. Chudley and R. J. Elliott, *Proceedings of the Physical Society (London)*, 1961, **77**, 353.

22 P. Hall and D. K. Ross, *Mol. Phys.*, 1981, **42**, 673.

23 K. Singwi and A. Sjölander, *Phys. Rev.*, 1960, **120**, 1093.

24 R. Hempelmann, *Quasielastic neutron scattering and solid state diffusion*, Clarendon Press, Oxford, 2000.

25 R. Hempelmann, C. Karmonik, T. Matzke, M. Cappadonia, U. Stimming, T. Springer and M. A. Adams, *Solid State Ion.*, 1995, **77**, 152–156.

26 T. Matzke, U. Stimming, C. Karmonik, M. Soetramo, R. Hempelmann and F. Güthoff, *Solid State Ion.*, 1996, **86-88**, 621–628.

27 M. Karlsson, M. E. Björketun, P. G. Sundell, A. Matic, G. Wahnström, D. Engberg, L. Börjesson, I. Ahmed, S. G. Eriksson and P. Berastegui, *Phys. Rev. B*, 2005, **72**, 094303: 1–7.

28 M. Karlsson, A. Matic, S. F. Parker, I. Ahmed, L. Börjesson and S. G. Eriksson, *Phys. Rev. B*, 2008, **77**, 104302.

29 R. Hempelmann, M. Soetratmo, O. Hartmann and R. Wäppling, *Solid State Ion.*, 1998, **107**, 269–280.

30 W. Münch, G. Seifert, K. D. Kreuer and J. Maier, *Solid State Ion.*, 1997, **97**, 39–44.

31 K. D. Kreuer, W. Munch, U. Traub and J. Maier, *Ber. Bunsenges. Phys. Chem.*, 1998, **102**, 552–559.

32 W. Münch, G. Seifert, K. D. Kreuer and J. Maier, *Solid State Ion.*, 1996, **86-88**, 647–652.

33 F. Shimojo, K. Hoshino and H. Okazaki, *J. Phys. Soc. Jpn.*, 1997, **66**, 8–10.

34 K. D. Kreuer, S. Adams, W. Münch, A. Fuchs, U. Klock and J. Maier, *Solid State Ion.*, 2001, **145**, 295–306.

35 Y. Yamazaki, F. Blanc, Y. Okuyama, L. Buannic, J. C. Lucio-Vega, C. P. Grey and S. M. Haile, *Nat. Mater.*, 2013, **12**, 647.

36 K. D. Kreuer, W. Münch, M. Ise, T. He, A. Fuchs, U. Traub and J. Maier, *Ber. Bunsenges. Phys. Chem.*, 1997, **101**, 1344.

37 K. D. Kreuer, *Solid State Ion.*, 1999, **125**, 285–302.

38 C. Karmonik, R. Hempelmann, J. Cook and F. Güthoff, *Ionics*, 1996, **2**, 69.

39 M. Pionke, T. Mono, W. Schweika, T. Springer and H. Schober, *Solid State Ion.*, 1997, **97**, 497–504.

40 B. Groß, C. Beck, F. Meyer, T. Krajewski, R. Hempelmann and H. Altgeld, *Solid State Ion.*, 2001, **145**, 325–331.

41 C. Beck, S. Janssen, B. Gross and R. Hempelmann, *Scripta Mater.*, 2001, **44**, 2309–2313.

42 D. Wilmer, T. Seydel and K. D. Kreuer, *Mater. Res. Soc. Proc.*, 2007, **972**, 15.

43 N. Malikova, C. K. Loong, J. M. Zanotti and F. Fernandez-Alonso, *J. Phys. Chem. C*, 2007, **111**, 6574–6580.

44 A. Slodczyk, P. Colomban, D. Lamago, M.-H. Limage, F. Raomain, S. Willemin and B. Sala, *Ionics*, 2008, **14**, 215–222.

45 M. Karlsson, I. Ahmed, A. Matic and S. Eriksson, *Solid State Ion.*, 2010, **181**, 126.

46 A. Braun, S. Duval, P. Ried, J. Embs, F. Juranyi, T. Strässle, U. Stimming, R. Hempelmann, P. Holtappels and T. Graule, *J. Appl. Electrochem.*, 2009, **39**, 262103.

47 P. Colomban, A. Slodczyk, D. Lamago, G. Andre, O. Zaafrani, O. Lacroix, S. Willemin and B. Sala, *J. Phys. Soc. Jpn.*, 2010, **79**, 1.

48 A. Slodczyk, P. Colomban, N. Malikova, O. Zaafrani, S. Longeville, J.-M. Zanotti, O. Lacroix and B. Sala, *Solid State Ion.*, 2013, **252**, 7–11.

49 Q. Chen, J. Banyte, X. Zhang, J. P. Embs and A. Braun, *Solid State Ion.*, 2013, **252**, 2–6.

50 M. Karlsson, D. Engberg, M. E. Björketun, A. Matic, G. Wahnström, P. G. Sundell, P. Berastegui, I. Ahmed, P. Falus, B. Farago, L. Börjesson and S. Eriksson, *Chem. Mater.*, 2010, **22**, 740–742.

51 M. Karlsson, P. Fouquet, I. Ahmed and M. Maccarini, *J. Phys. Chem. C*, 2010, **114**, 3293.

52 N. Jalarvo, L. Stingaciu, D. Gout, Z. Bi, M. P. Paranthaman and M. Ohl, *Solid State Ion.*, 2013, **252**, 12.

53 R. Kolhrausch, *Annu. Phys. (Weinheim, Ger.)*, 1854, **1**, 179.

54 G. Williams and D. C. Watts, *Trans. Faraday Soc.*, 1970, **66**, 80.

55 M. Karlsson, A. Matic, C. S. Knee, I. Ahmed, L. Börjesson and S. G. Eriksson, *Chem. Mater.*, 2008, **20**, 3480–3486.

56 N. Jalarvo, O. Gourdon, Z. Bi, D. Gout, M. Ohl and M. P. Paranthaman, *Chem. Mater.*, 2013, **25**, 2741.

57 F. M. Piegsa, M. Karlsson, B. van den Brandt, C. J. Carlile, E. M. Forgan, P. Hautle, J. A. Konter, G. J. McIntyre and O. Zimmer, *J. Appl. Cryst.*, 2013, **46**, 30–34.